Design and optimization of supersonic turbines for detonation combustors

Jorge SOUSA [a], **Elena COLLADO-MORATA** [b], **Guillermo PANIAGUA** [c,*]

[a] *Flemish Institute for Technological Research, Mol 2400, Belgium*
[b] *Commissariat à l'énergie atomique et aux énergies alternatives, Le Barp 33114, France*
[c] *Mechanical Engineering, Purdue University, West-Lafayette IN 47906, USA*

Abstract Detonation-based engines offer a potential surge in efficiency for compact thermal power systems. However, these cycles require ad-hoc components adapted to the high outlet velocity from the detonation combustors. This paper presents the design methodology of turbine stages suitable for supersonic inlet conditions and provides a detailed analysis of optimized turbine geometries. A reduced-order solver examines the supersonic blade rows' functional design space, quantifies the turbine's non-isentropic performance, and budgets the turbine loss for different optimized leading-edge designs and chord to pitch ratios. The shock-wave interactions were identified as the predominant contributor to turbine losses, and optimal pitch-chord ratios were determined for various inlet Mach numbers. Finally, with this tool, the specific-power output for a wide range of design configurations was computed; and the metal angle that ensures flow starting and maximizes power extraction was calculated. The detailed numerical study describes the flow interactions in a supersonic turbine and offers new correlations to guide the design of future supersonic turbines.
© 2022 Chinese Society of Aeronautics and Astronautics. Production and hosting by Elsevier Ltd. This is an open access article under the CC BY-NC-ND license (http://creativecommons.org/licenses/by-nc-nd/4.0/).

1. Introduction

Gas turbines have played a significant part in advancing air-transport technology by improving comfort while reducing the time between distant human settlements. However, the

* Corresponding author.
E-mail addresses: gpaniagua@purdue.edu, gpaniagua@me.com (G. PANIAGUA).

steady growth in air transportation, increasing by 5% per year,[1] doubles the expected annual improvements in engine-specific fuel consumption.[2] Globalization and environmental concerns drive the need for minimal pollutant emissions,[3] compelling new efficient propulsion architectures.[4] In detonation-based engines[5] combustors burn hydrogen through a detonation process instead of the conventional deflagration reaction. The fusion of this type of combustor with a short nozzle and a supersonic turbine[6] is shown in Fig. 1(a). Numerous authors have presented increased cycle efficiency, first using steady assumptions[7,8] and, more recently, reduced-order models.[6,9,10] Several other authors have demonstrated the performance and the aero-thermal challenges associated with turbine stages operating with detonation combustors.[11–13] The
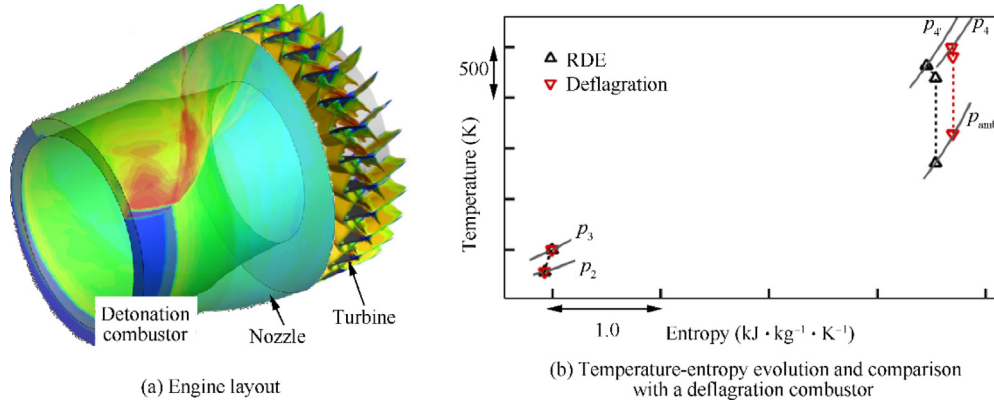
(a) Engine layout

(b) Temperature-entropy evolution and comparison
with a deflagration combustor

Fig. 1 Rotating detonation engine architecture and performance with an axial supersonic turbine.

iso-temperature contours reveal the rotating detonation front, resulting in a sudden increase in pressure consuming the hydrogen-air mix at supersonic velocities along the tangential clock-wise direction. An oblique shock wave and a slip line are anchored at the triple point and propagate towards the combustor outlet into the nozzle and supersonic turbine. Recent experimental and numerical research[5,14] demonstrates that the unsteady flow downstream of the Rotating Detonation Combustor (RDC) lies within the low supersonic range.[15–17] Hence, shock waves are generated at the airfoil leading-edges, creating numerous aerodynamic and heat transfer challenges.

Fig. 1(b) is a temperature-entropy diagram that compares two small pressure ratio turbojets;[6] a Rotating Detonation-combustor Engine (RDE, black delta symbol) with a conventional deflagration Brayton engine (red gradient symbol). Both engines have an identical compression ratio, with the same combustor inlet conditions p_3 and T_3 (p is the pressure and T is the temperature). However, the detonation combustor presents a higher outlet pressure ($p_{4'} > p_4$), although a slightly lower average outlet temperature, due to the temperature fluctuations. The higher total pressure is also associated with a lower entropy generation, while the enthalpy drop across the turbine is the same in both engines. Therefore, the pressure downstream of the turbine stage remains higher in the detonation engine, increasing the turbojet thrust. Hence, detonation engines offer a potential leap in terms of overall engine performance.

This paper focuses on analyzing a new class of supersonic-axial turbines instead of the traditional subsonic turbines designed for low inlet Mach numbers of about 0.2.[18] A turbine passage reduces the area along the axial direction. For a supersonic inlet condition, the flow is gradually decelerated up to the throat. During the starting phase of the engine, the flow transits from a subsonic to a supersonic operation. A normal shock wave must travel from the combustor to the turbine outlet following a sequence outlined in Fig. 2 below. At time 0.3 ms, one can observe a normal shock wave between the inlet and the leading-edges. The supersonic flow entering the turbine passage is defined by the conditions after this normal shock wave. Hence, only if the post-shock flow is not chocked at the throat, the shock wave can progress further downstream. Between 0.6 ms and 0.9 ms, the shock begins a complex interaction with the leading-edge and the airfoil walls, and a complex leading-edge oblique shock system is created. Downstream of the trailing-edge, the oblique shocks converge into a normal shock

transported towards the outlet. After 2.7 ms, the traveling shock wave arrives at the outlet, and a steady-state is achieved.

Fig. 3(a) sketches the two-dimensional supersonic turbine passage, defined by the inlet and outlet area (A) and the inlet/outlet flow angle (α). The area can be expressed as a function of outlet flow angle (α), the pitch (g), and channel height (H): $A = g\cos\alpha H$. The contraction ratio from the inlet to the throat must be limited to ensure that all the flow can pass through the throat. To ensure self-staring, following Kantrowitz and Donaldson,[19] the throat must be sufficiently large to ensure that all the mass flow can be swallowed with the conditions after the starting shock wave. Hence, the turning across the turbine passage must be limited to ensure that the contraction ratio A_{out}/A_{in}, is above the Kantrowitz limit defined in Eq. (1), denoted as "design space" in Fig. 3(b), all the turbines design above the Kantrowitz limit will be self-starting for a sudden change of conditions from subsonic into supersonic.

$$\left.\frac{A_{out}}{A_{in}}\right|_{Kantr.} = \frac{1}{Ma_{in}}\left[\frac{(\gamma+1)Ma_{in}^2}{(\gamma-1)Ma_{in}^2+2}\right]^{\frac{\gamma}{\gamma-1}}$$

$$\cdot \left[\frac{\gamma+1}{2\gamma Ma_{in}^2-(\gamma-1)}\right]^{\frac{1}{\gamma-1}}\left(\frac{1+\frac{\gamma-1}{2}Ma_{in}^2}{\frac{\gamma+1}{2}}\right)^{\frac{\gamma-1}{2(\gamma-1)}} \quad (1)$$

where Ma_{in} is the inlet Mach number, and γ is the isentropic expansion factor or isentropic exponent for an ideal gas ($\gamma = c_p/c_v$, c_p specific heat capacity at constant pressure, and c_v the specific heat capacity at constant volume). Hence, Eq. (2) shows the allowable outlet conditions can be computed to respect the Kantrowitz limit.

$$\alpha_{out} < \arccos\left(\left.\frac{A_{out}}{A_{in}}\right|_{Kantr.} \cdot \frac{H_{in}}{H_{out}}\cos\alpha_{in}\right) \quad (2)$$

A methodology to optimize the stator and rotor's metal angles was developed conducive to maximum non-isentropic power output. We evaluated the losses and studied the impact of different chord-to-pitch ratios, leading-edge shape, rotational speed, and end-walls design to achieve this goal. The performance predictions were validated against calibrated 3D Reynolds-Averaged Navier-Stokes simulations. Finally, we present a range of design parameters that minimize the supersonic turbine's losses. The stator/turbine unstarting constrains the design space. After the design parameters are selected. The method of characteristics coupled with the optimization algorithm[20] is used to optimize the shape of the supersonic tur-
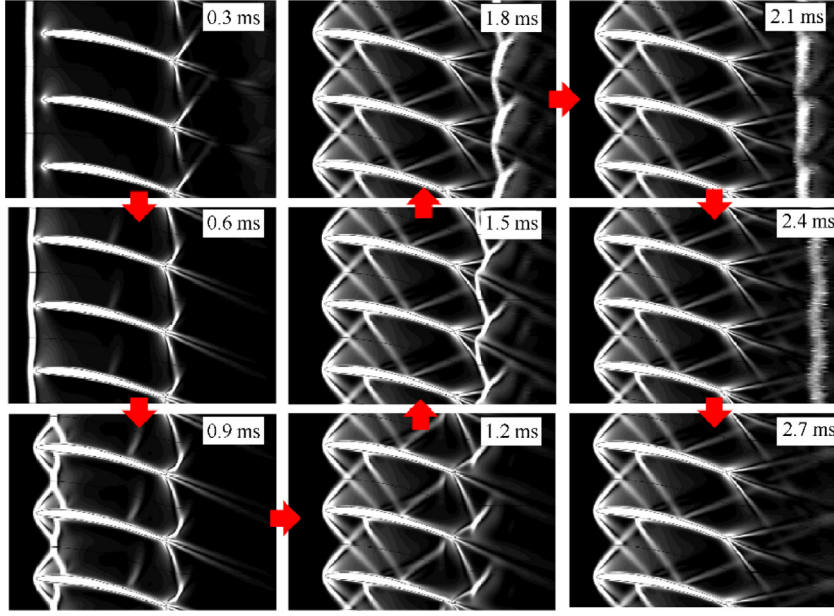
Fig. 2 Starting sequence using schlieren visualizations at different instants across a supersonic turbine.

(a) Turbine passage sketch

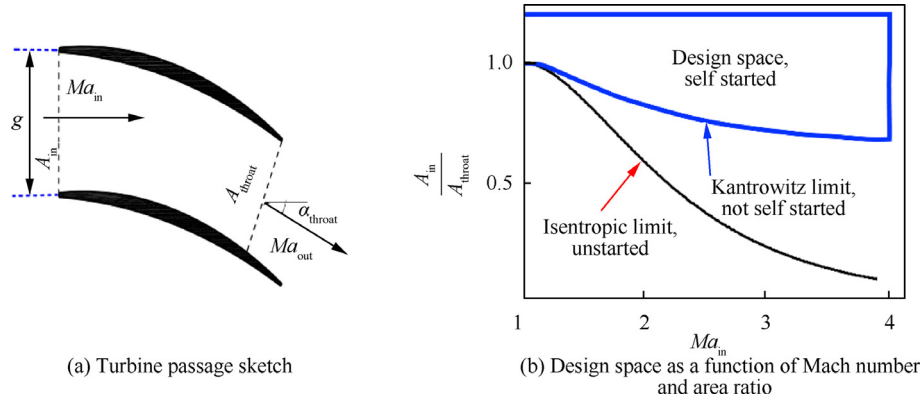(b) Design space as a function of Mach number and area ratio

Fig. 3 Definition of self-started passage.

bine passage. The impact of pulsating flow is then quantified with unsteady Reynolds-averaged Navier-Stokes simulations.[21,22]

2. Computational tool

The three-dimensional flow field across the supersonic passages was retrieved by solving the Reynolds-Average Navier-Stokes (RANS) equations with the numerical solver CFD+ + 14.1.1 developed by Metacomp Technologies. The governing Navier-Stokes equations are expressed as:

$$\frac{\partial \boldsymbol{Q}}{\partial t} + \frac{\partial (\boldsymbol{F}_1 + \boldsymbol{G}_1)}{\partial x} + \frac{\partial (\boldsymbol{F}_2 + \boldsymbol{G}_2)}{\partial y} + \frac{\partial (\boldsymbol{F}_3 + \boldsymbol{G}_3)}{\partial z} = 0 \quad (3)$$

where $\boldsymbol{Q}$ represents the dependent variables, $\boldsymbol{F}$ the inviscid flux vectors, $\boldsymbol{G}$ the viscous flux vectors. In our steady-state simula-

tions, the first term on the left-hand side is zero, there are no source terms.

$$\boldsymbol{Q} = \begin{bmatrix} e \\ \rho \\ \rho u \\ \rho v \\ \rho w \end{bmatrix}, \boldsymbol{F}_1 = \begin{bmatrix} u(e+p) \\ \rho u \\ \rho u^2 + p \\ \rho vu \\ \rho wu \end{bmatrix},$$

$$\boldsymbol{F}_2 = \begin{bmatrix} v(e+p) \\ \rho v \\ \rho vu \\ \rho v^2 + p \\ \rho wv \end{bmatrix}, \boldsymbol{F}_3 = \begin{bmatrix} w(e+p) \\ \rho w \\ \rho uw \\ \rho vw \\ \rho w^2 + p \end{bmatrix}$$

where e is the specific energy, ρ is density, u the velocity in the axial direction, v the velocity in the tangential direction and w the flow velocity in the radial direction.

$$\mathbf{G}_1 = \begin{bmatrix} \dot{q}_x - u\tau_{xx} - v\tau_{xy} - w\tau_{xz} \\ 0 \\ -\tau_{xx} \\ -\tau_{xy} \\ -\tau_{xz} \end{bmatrix},$$

$$\mathbf{G}_2 = \begin{bmatrix} \dot{q}_y - u\tau_{yz} - v\tau_{yy} - w\tau_{yz} \\ 0 \\ -\tau_{xy} \\ -\tau_{yy} \\ -\tau_{yz} \end{bmatrix}, \qquad (4)$$

$$\mathbf{G}_3 = \begin{bmatrix} \dot{q}_z - u\tau_{zx} - v\tau_{zy} - w\tau_{zz} \\ 0 \\ -\tau_{xz} \\ -\tau_{yz} \\ -\tau_{zz} \end{bmatrix}$$

In Eq. (4) the flux vectors of Eq. (3) are represented. The first row represents energy balance (where $e = c_v T$ and $p = \rho R T$, R is the ideal gas constant). The continuity equation is expressed in the second line. The last three rows are accountable for the Navier-Stokes equations, where τ_{ij} is the shear stress tensor component and $\dot{q}_i$ denotes the heat flux ($\dot{q}_i = -\bar{k}\frac{\partial T}{\partial x_i}$, $\bar{k}$ is the thermal conductivity). A density-based algorithm is used to accommodate for compressibility effects. The Spalart-Allmaras (SA) closure[23] was added for the turbulence modelling, where the shear stress tensor component τ_{ij} in Eq. (4) is formulated as follows:

$$\tau_{ij} = v_t S_{ij}, \; S_{ij} = \left(\frac{\partial u_i}{\partial x_j} + \frac{\partial u_j}{\partial x_i} - \frac{2}{3} \cdot \frac{\partial u_k}{\partial x_k} \delta_{ij} \right)$$

where δ_{ij} is the Kronecker delta operator and the kinematic eddy viscosity is defined as:

$$v_t = \widetilde{v} f_{v1}, \; f_{v1} = \frac{\chi^3}{\chi^3 + c_{v1}^3}, \; \chi \equiv \frac{\widetilde{v}}{\upsilon}$$

where $\widetilde{v}$ is the working variable of the turbulence model, c_{v1} is a constant (define below with all the constants), υ is the molecular kinematic viscosity. Hence, an additional equation needs to be solved for $\widetilde{v}$. Since in our simulations, no rotation was included, and we assumed a fully turbulent boundary layer the transport equation for $\widetilde{v}$ is:

$$\frac{\partial}{\partial x_j}\left(u_j \widetilde{v} \right) = c_{b1} \left\{ (1 + c_{r1}) \frac{2r^*}{1 + r^*} \left[1 - c_{r3} tan^{-1} \left(c_{r2} \widetilde{r} \right) \right] - c_{r1} \right\} (1 - f_{t2}) \widetilde{S} \widetilde{v}$$
$$+ \frac{1}{\sigma} \left\{ \nabla \cdot \left[\left(v + \widetilde{v} \right) \nabla \widetilde{v} \right] + c_{b2} \left(\nabla \widetilde{v} \right)^2 \right\}$$
$$- \left(c_{w1} f_w - \frac{c_{b1}}{\kappa^2} f_{t2} \right) \left(\frac{\widetilde{v}}{d} \right)^2 \qquad (5)$$

where,

$$r^* = \frac{\hat{S}}{\omega}, \; \widetilde{r} = \frac{2\omega_{ik}\hat{S}_{jk}}{\hat{D}^4}\left(\frac{\mathrm{D}\hat{S}_{ij}}{\mathrm{D}t}\right), \; \hat{S}_{ij} = \frac{1}{2}\left(\frac{\partial u_i}{\partial x_j} + \frac{\partial u_j}{\partial x_i}\right),$$
$$\omega_{ij} = \frac{1}{2}\left(\frac{\partial u_i}{\partial x_j} - \frac{\partial u_j}{\partial x_i}\right), \; \hat{D}^2 = \frac{1}{2}\left(2\hat{S}_{ij}\hat{S}_{ij} + 2\omega_{ij}\omega_{ij}\right),$$
$$\hat{S}^2 = 2\hat{S}_{ij}\hat{S}_{ij}, \; \omega = 2\omega_{ij}\omega_{ij}$$

The sink term in Eq. (5) involves the following terms:

$$f_w = g\left(\frac{1 + c_{w3}^6}{g^6 + c_{w3}^6}\right)^{1/6}, \; g = r\left[1 + c_{w2}\left(r^5 - 1\right)\right], \; r = \frac{\widetilde{v}}{\widetilde{S}(\kappa d)^2},$$

$$\widetilde{S} = \omega + \frac{\widetilde{v}}{(\kappa d)^2}\left(1 - \frac{\chi}{1 + \chi f_{v1}}\right), \; f_{t2} = c_{t3}e^{-c_{t4}\chi^2}$$

d is the distance to the wall and v the kinematic molecular viscosity. The model constants are the following:

$c_{b1} = 0.1355, \sigma = 2/3, \quad c_{b2} = 0.622, \quad \kappa = 0.41,$
$c_{w1} = \frac{c_{b1}}{\kappa^2} + \frac{1+c_{b2}}{\sigma}, \; c_{w2} = 0.3,$
$c_{w3} = 2, \quad c_{v1} = 7.1, \quad c_{t3} = 1.1, \quad c_{t4} = 2, \quad c_{r1} = 1.0,$
$c_{r2} = 12.0, c_{r3} = 1.0.$

The thermodynamic properties are obtained utilizing temperature-dependent coefficients in a real gas model.[24] The viscosity of air was computed based on the Sutherland Law with the following coefficients (T_{ref} = 273.11 K, $\sigma_{\text{viscosity}}$ = 1.716 × 10^{-5} kg/(m·s), $C_{\text{viscosity}}^{\text{te}}$ = 111.0, $k_{\text{conductivity,ref}}$ = 2.41 × 10^{-3} kg·m/s^3 and $C_{\text{conductivity}}^{\text{te}}$ = 194). The finite volume method is used for spatial discretization, with all control volumes being cell-centered. The inviscid flux function was a second-order upwind scheme using a Harten-Lax-Van Leer-Contact (HLLC) Riemann solver.[25] The spatial variables' interpretation is performed through a second-order Total Variation Diminishing (TVD) polynomial interpolation with a continuous limiter for stability. The solver with the same numerical setup was validated against experimental data from a transonic turbine evaluated by Sousa and Paniagua.[20] The numerical domains were discretized with the software AutoGrid5. Only one passage was numerically computed by applying periodicity at the two sides of the computational domain in the tangential direction. Fig. 4(a) shows an example of the 3D structured grid with multi-block meshes. The boundary layer is discretized and solved up to the wall. Static inlet conditions are imposed at the inlet, and a supersonic state is set at the outlet. A grid sensitivity study was conducted to analyze the mesh dependency of the solution. Fig. 4(b) plots the results of the ratio of the outlet total pressure to the inlet total pressure ($p_{0,\text{out}}/p_{0,\text{in}}$) probed at $0.5C_{\text{ax}}$ (C_{ax} is the airfoil axial chord) downstream of the trailing-edge ($x = x_{\text{te}} + 0.5C_{\text{ax}}$, x_{te} is the axial coordinate of the airfoil trailing edge) for three grid levels (coarse-Grid N_3, medium-Grid N_2, and fine-Grid N_1). $R\theta$ is the arc-lenght along the tangential direction.

To evaluate the grid convergence, we used the Richardson extrapolation method[26] to compute the Grid Convergence Index (GCI) as recommended by Celik et al.[27] Table 1 summarizes the three different grids' results, with a refinement ratio (r) close to the recommended value of 1.3. The quantity of interest was the total pressure ratio ($p_{0,\text{out}/}$ $p_{0,\text{in}}$). These values were used to estimate the order of accuracy ($\widetilde{p} = 1.7$), close to the used 2nd order discretization scheme. To quantify the relative uncertainty ($e_{\text{rel.}}$) the Richardson extrapolation is applied, plus extrapolated uncertainty ($e_{\text{ext.}}$). Finally, we defined the GCI as $\text{GCI} = \frac{1.25e_{\text{rel.}}}{r^{\widetilde{p}} - 1}$. Based on these results, we selected Grid N_2 for its little uncertainty and lower computational times than Grid N_3. Advanced convergence acceleration techniques used include unique pre-conditioning, relaxation, and multi-grid algorithms.
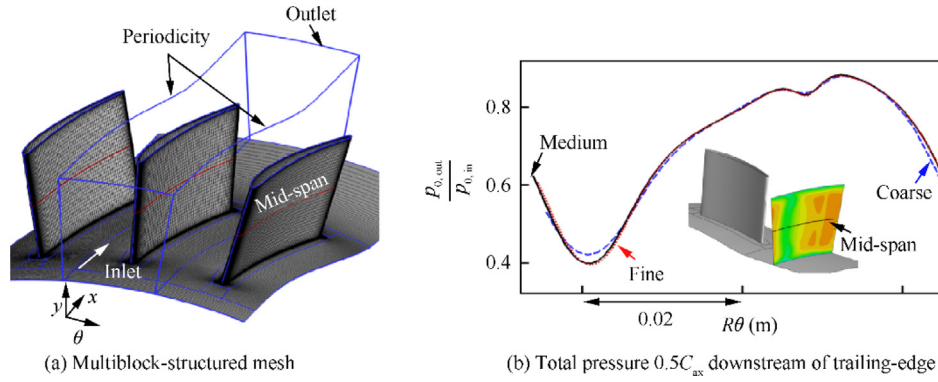
Fig. 4 Computational domain.

Table 1 Summary of discretization error analysis.

Item	Size	r	$e_{rel.}$ (%)	$e_{ext.}$ (%)	GCI (%)
Grid N_1	3197952				
Grid N_1/Grid N_2		1.33	0.41	0.64	0.81
Grid N_2	1333248				
Grid N_2/Grid N_3		1.47	0.035	0.36	0.045
Grid N_3	419968				

3. Aerodynamic performance

3.1. Development of a shock and viscous loss prediction tool

The supersonic flow pattern in turbine airfoils is shown in Fig. 5(a). Strong leading-edge bow shock waves propagate throughout the passage due to reflections creating total pressure loss ($p_0(x)$). Additionally, the boundary layer develops along the airfoil; due to the turning, a supersonic diffuser is created, magnifying the viscous layer loss, usually called profile losses. The boundary layer then detaches at the trailing-edge and begins a mixing process. The present reduced-order model considers both the inviscid contribution arising from the leading-edge shock waves as well as the viscid loss created by the profile and mixing losses. In Fig. 5(b), particles flowing

from Point A to Point B are first submitted to the leading-edge bow shock, followed by the combined effect of the boundary layer growth and reflected shock as the particles travel from Point B to Point C. However, this analysis does not consider other losses created by the trailing-edge shock system interacting with the wakes and secondary flows. Still, they represent a significant contribution in low aspect ratio supersonic profiles.[13]

To characterize the detached leading-edge bow shock, we utilized the Moeckel empirical method.[28] Fig. 6(a) sketches the leading-edge bow shock profile. SB is the sonic point along the leading-edge, while θ_d represent the detachment angle for the given inlet Mach (Ma_{in}). Upstream of the leading-edge, the shock wave geometry follows an asymptotic line, with β function of the incoming Mach number, defined by Moeckel with Eq. (6).
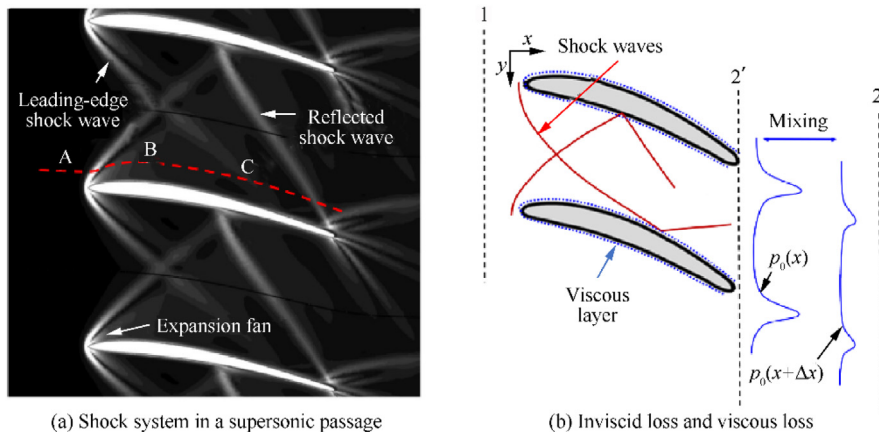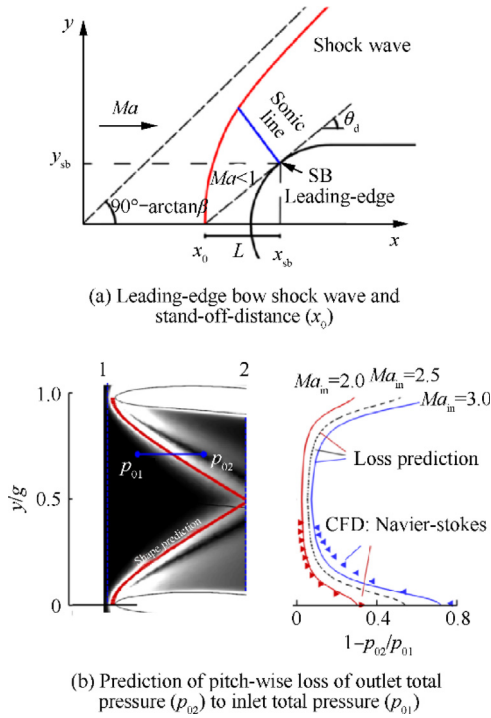

Fig. 5 Flow topology and losses in a supersonic blade passage.

(a) Leading-edge bow shock wave and
stand-off-distance (x_0)

(b) Prediction of pitch-wise loss of outlet total
pressure (p_{02}) to inlet total pressure (p_{01})

Fig. 6   Leading edge shock reduced-order model.

$$y_{\text{shock}} = \frac{\left(x_{\text{shock}}^2 - x_0^2\right)^{1/2}}{\beta} \qquad (6)$$

where x_{shock} and y_{shock} are the coordinates of the shock wave while, x_0 is the axial coordinate of the shock inception.

A study was conducted to analyze the shape of the reduced-order model results of the leading-edge bow shock geometry and benchmark against the CFD results as a function of inlet Mach numbers. Fig. 6(b) compares the estimated shock wave profile, red line, with a numerical schlieren visualization of the CFD results, depicted in grayscale. To study where the entropy is generated, the loss gradient in the pitch-wise direction across one passage (g = pitch) is plotted in Fig. 6(b) right for three Mach numbers. The maximum of entropy is achieved at the edge of the passage ($y = 0, g$). In this region shock wave is perpendicular to the flow.

Both profile and mixing losses are correlated and are evaluated by applying a mass balance[29] between Plane 2′ and Plane 2, which particularized for supersonic passages yield Eq. (7):

$$\cos\alpha_{2'}(1 - \delta^* - \delta_{\text{te}})(\rho V)_{2'} = \cos\alpha_2(\rho V)_2 \qquad (7)$$

where V is the magnitude of the local flow velocity. The balance of axial and tangential momentum results in Eqs. (8) and (9):

$$\sin\alpha_{2'}\cos\alpha_{2'}\left(1 - \delta^* - \delta_{\text{te}} - \theta^*\right)\left(\rho V^2\right)_{2'} = \sin\alpha_2\cos\alpha_2\left(\rho V^2\right)_2 \quad (8)$$

$$gp_{2'} + \cos^2\alpha_{2'}\left(1 - \delta^* - \delta_{\text{te}} - \theta^*\right)\left(\rho V^2\right)_{2'}$$
$$= gp_2 + \cos^2\alpha_2\left(\rho V^2\right)_2 \qquad (9)$$

where δ_{te} is the ratio of trailing-edge thickness to throat area ($t/(g\cos\alpha_{2'})$); $\delta^* = (\delta_{\text{ss}} + \delta_{\text{ps}})/(g\cos\alpha_{2'})$ is the boundary layer displacement, where $\delta_{\text{ss}}, \delta_{\text{ps}}$ the displacement at the suction and pressure side respectively; $\theta^* = \left(\theta_{\text{ss}} + \theta_{\text{ps}}\right)/(g\cos\alpha_{2'})$ repre-
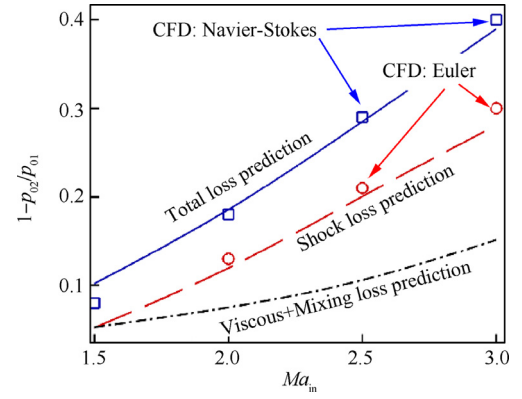
Fig. 7   Viscous, shock wave and total losses (compared with Euler and Navier-Stokes simulations).
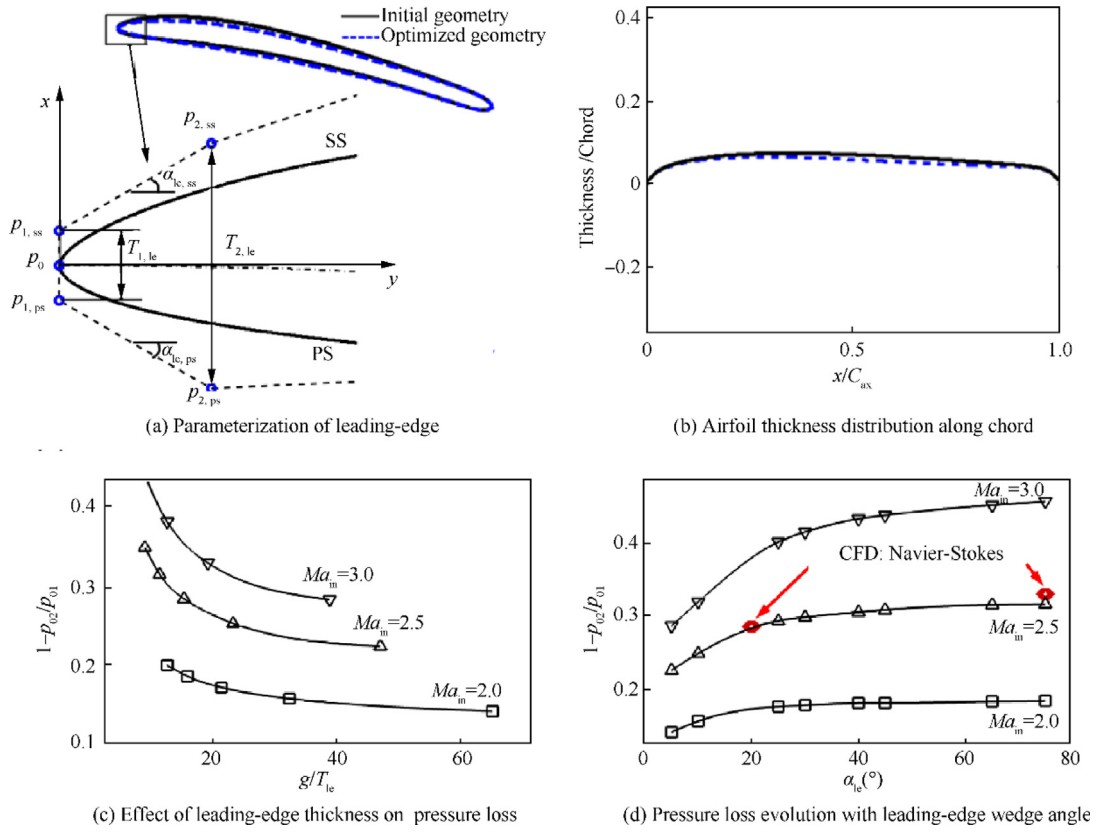
sent the momentum thickness at the trailing-edge where, θ_{ss} and θ_{ps} are the momentum thickness at the suction and pressure side respectively. The empirical correlation outlined by Stratford and Beavers[30] was used to compute those thicknesses.

3.2. Assessment of loss models

Fig. 7 depicts the total loss prediction, $1 - p_{02}/p_{01}$ (solid blue line); the corresponding viscous contribution (black dashed-dotted line) from the mixing and profile; the leading-edge bow shock losses (red dashed line). To assess the methodology, Fig. 7 also includes the results from the higher-order two-dimensional numerical simulations. The red circular symbols represent the non-viscous (Euler) simulations, while the blue squared symbols represent the Navier-Stokes simulation. The agreement between the Computational Fluid Dynamics simulations (CFD) and the shock and total loss prediction is within 2% and 5%, respectively. The most significant contribution to loss is caused by shock waves, which increase dramatically as the inlet Mach number is increased. For the selected aspect ratio (height to chord). The contribution to entropy generation of the trailing-edge shock system or secondary flows are marginal for the selected aspect ratio (height to chord); and consequently are neglected in the frame of this analysis. For high chord to height ratios, the endwall effects dominate, as demonstrated for the non-optimal chord to pitch ratios.[13]

3.3. Effect of leading-edge design

The main contribution of this methodology is to quickly perform evaluations over a large span design space with a heterogeneous turbine profile topology. We ran several viscous simulations to evaluate the current methodology's ability to predict the losses' values and derivatives for comparison purposes. This reduced-order tool was coupled with a genetic algorithm to optimize the turbine passages using a low number of design parameters.[20] The camber line was built using a quadratic Bezier curve. Among the free design parameters, we have the leading-edge thickness $T_{1,\text{le}}$ in Fig. 8(a), and the wedge leading-edge angle α_{le}. Fig. 8(b) presents the thickness to chord distribution along the axial direction for the baseline and optimized geometry. Fig. 8(c) shows that large leading-

(a) Parameterization of leading-edge

(b) Airfoil thickness distribution along chord

(c) Effect of leading-edge thickness on pressure loss

(d) Pressure loss evolution with leading-edge wedge angle
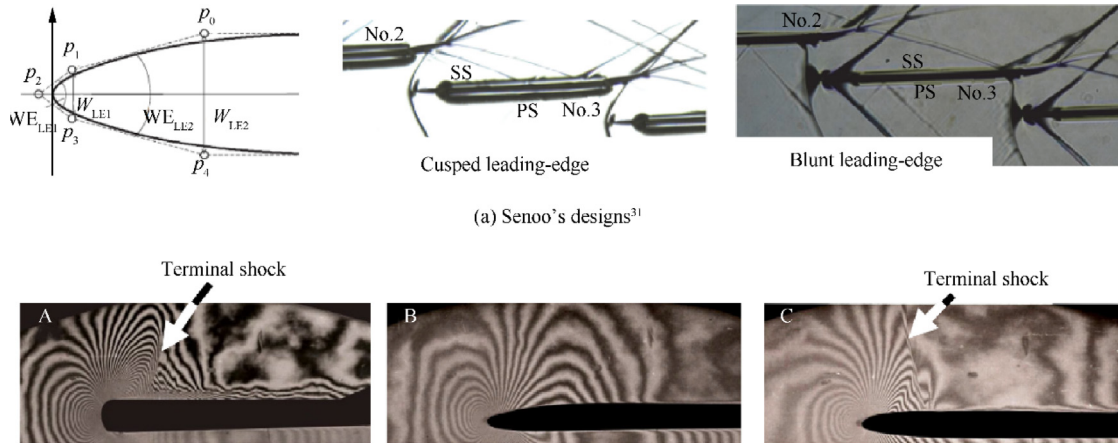
Fig. 8 Leading edge and thickness geometry definition and impact on total pressure loss.
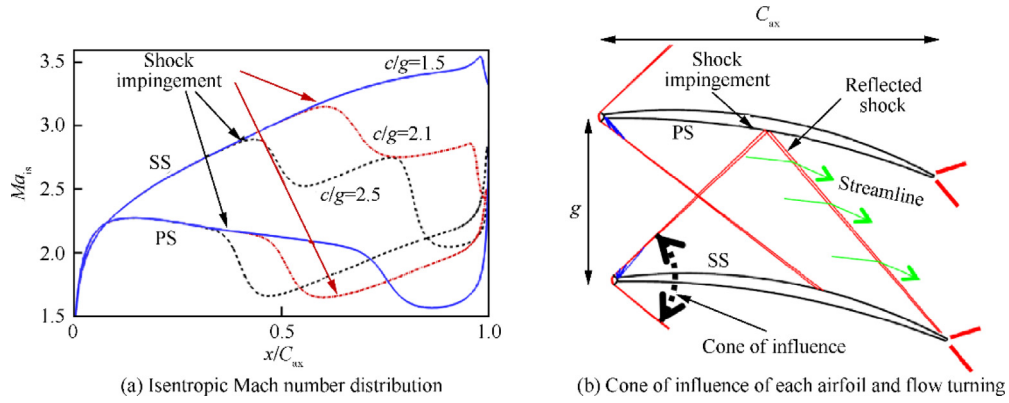
edge thickness induces a surge in the losses for thick airfoils. The leading-edge design determines the bow shock's location ahead of the leading-edge, the prime contribution to the loss generation. Fig. 8(d) shows that diminishing the wedge angle cause a decrease in the shock losses. Therefore, the mechanical constraints are to be balanced with the aerodynamic penalty.

In the last stage of steam turbines, due to the high-peripheral speeds, we also observe supersonic flows near the tip in the relative frame of reference but with a subsonic axial component. The design and optimization of such profiles are essentially focused on optimizing the leading-edge region

where shock waves are generated. The optimized results obtained by Senoo[31] are shown in Fig. 9(a); similarly to our conclusion, the cusped airfoil presents a leading-edge shock wave with a narrower angle that helps to minimize the shock strength and their consequent interaction with the boundary layer of the neighborhood blade. Šafařík's team designed multiple supersonic turbine airfoils. Based on the interferometric results,[32] we note the appearance of a terminal shock in Profile A and Profile C due to the over acceleration around the leading-edge. Design B with a cusped geometry allowing to eliminate the terminal shock.

(a) Senoo's designs[31]

(b) Šafařík's interferometric measurements of supersonic tips with a shock-free design (Design B)[32]

Fig. 9 Leading-edge geometries of supersonic steam turbine rotor tips.

(a) Isentropic Mach number distribution

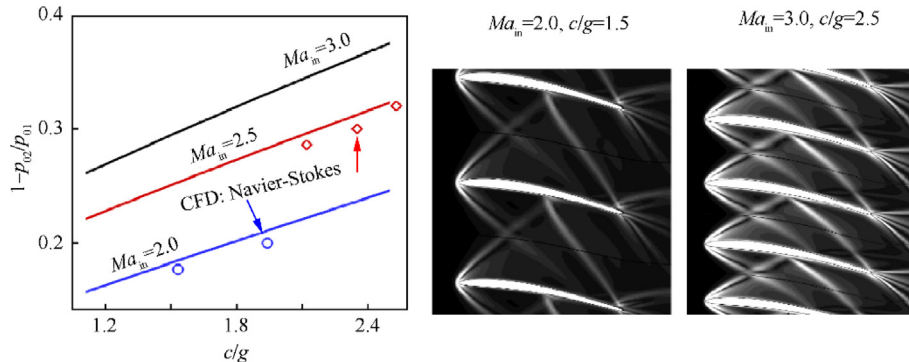(b) Cone of influence of each airfoil and flow turning

Fig. 10   Supersonic airfoil loading.

3.4. Effect of chord to pitch ratio

Fig. 10(a) displays the isentropic Mach number (Ma_{is}) along the airfoil's pressure and suction side for the three pitch to chord ratios. The flow accelerates rapidly to sonic conditions near the stagnation region. A Prandtl-Mayer expansion around the leading-edge further accelerates the flow to supersonic conditions. The acceleration continues along the suction side due to the convex curvature, while a smoother deceleration occurs along the pressure side due to its concave curvature. Around the airfoil leading-edge, all the Mach number lines overlap, as in this region, the flow is outside of the zone of influence of the neighbor airfoil, as sketched in Fig. 10(b). The first traceable impact of the neighborhood blade is the first shock impingement. For the chord-to-pitch $c/g = 1.5$, no Suction Side (SS) shock impingement can be identified on the Mach number distribution. Therefore, this part of the airfoil operates without any flow influence from the neighborhood airfoil. The shock impingement appears on both sides of the airfoil and moves incrementally upstream, increasing the chord to pitch ratio. At this location, a reflected shock wave is generated and propagated downstream. For $c/g = 2.1$, the reflected shock from the pressure side impacts close to the trailing-edge, as exemplified in Fig. 10(b). While for $c/g = 2.5$ this shock wave interacts again with the suction side, as seen by the Mach number abatement at around $x/C_{ax} = 0.75$, the loading is inverted.

Fig. 11 shows the predicted total pressure loss in function of the chord to pitch ratio (c/g) at three inlet Mach numbers.
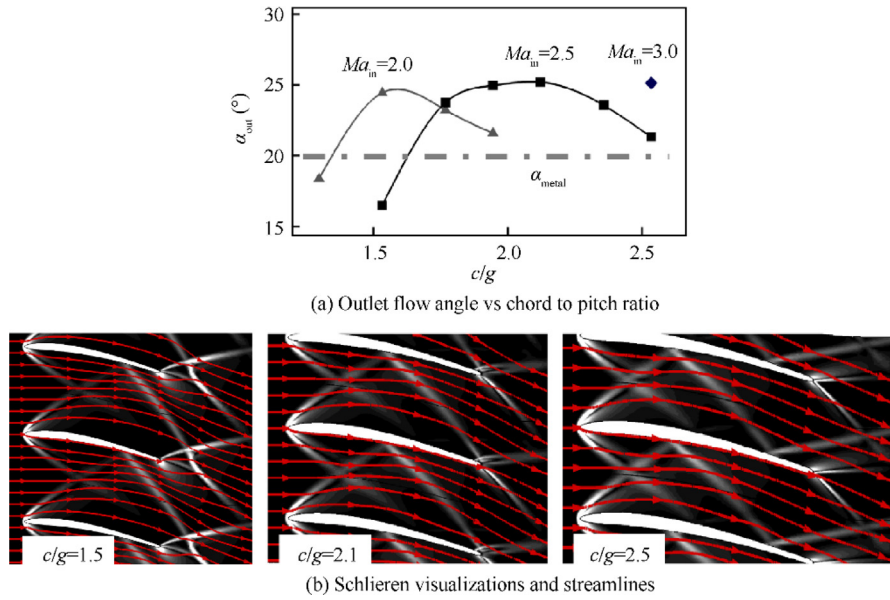
Several Navier-Stokes simulations are also included in Fig. 11 to reassess the validity of the reduced-order model to assess the passage loss. For a given pitch, we note a monotonic increase of the loss with the chord. At $Ma_{in} = 2.0$, a 10% change on the chord to pitch ratio results in approximately 5% variation in total pressure loss. Fig. 10(a) evidence that a higher chord to pitch ratio is conducive to two shock waves impacting the suction side.

To evaluate the optimal c/g ratio, the outlet flow angle (α_{out}) was mass flow averaged at a plane located $0.5C_{ax}$ downstream of the trailing-edge. Fig. 12(a) represents outlet flow angle as a function of the c/g ratio for several inlet Mach numbers. One can observe the existence of an optimal c/g at which the outlet flow angle is maximized, in fact exceeding the metal angle by approximately 5°. This occurs precisely for a configuration where the reflected shock from the suction side impinges on the trailing edge, as seen in Fig. 12(b) for $c/g = 2.1$, Fig. 12(a) reveals that the optimal c/g rises with the Mach number due to the narrower cones of influence seen in Fig. 12(b). Hence, the c/g pitch ratio needs to be adapted to obtain the same shock features. Accordingly, the optimal c/g correlates with the Mach number for an outlet metal angle of 20°. as, $c/g = Ma_{in} - 0.5$.

Fig. 13 evaluates the outlet Mach number (Ma_{out}) and flow angle (α_{out}) for three c/g values. At low c/g (Fig. 13(a)), the lack of flow guidance across the passage induces an important velocity step at the trailing-edge that promotes the appearance of a strong shock wave and an expansion fan. Consequently, the downstream flow presents high pitch-wise velocity gradi-


Fig. 11   Total pressure loss prediction at three Mach numbers.

(a) Outlet flow angle vs chord to pitch ratio

(b) Schlieren visualizations and streamlines

Fig. 12   Effect of chord to pitch ratio on outlet flow angle and flow structures.

(a) c/g=1.3

(b) c/g=1.5

(c) c/g=1.9
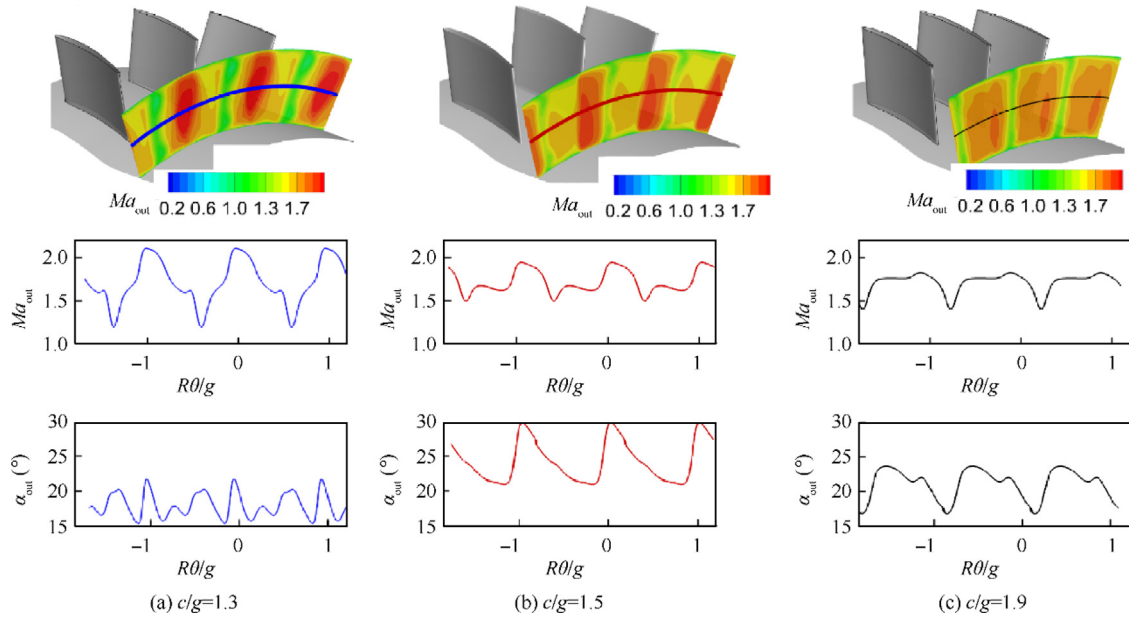
Fig. 13   Downstream conditions for several chord to pitch ratios.

ents. In this case, the Mach number fluctuates around 0.45, which denotes 30% of the mean outlet value. Regarding the flow angle, its mean value (α_{out}) is below the metal angle (α_{metal}) and the fluctuations are within 3°. For the test case with c/g = 1.5, Fig. 13(b), a decrease in the Mach number amplitudes (Ma = ±0.25) is shown, while the mean value of the flow angle is considerably higher (α_{out} = α_{metal} + 4.4°). The flow angle fluctuations present a lower spatial frequency content; however, the amplitude is increased to ±4°. From

the iso-contour in Fig. 13(c), it appears that the better flow guidance, in this configuration, provides a more homogenous flow field; nonetheless, the amplitudes of the mid-span Mach number are similar to the previous case. Due to the airfoils' additional flow guidance, the mean flow angle gets closer to the metal angle, and the extra turning provided by the shock wave is smeared out. From this analysis, it appears that c/g = 1.5 for the Ma_{in} = 2, represents an optimal value that could allow a higher work extraction in the downstream row.

(a) Velocity triangles

(b) Meridional view
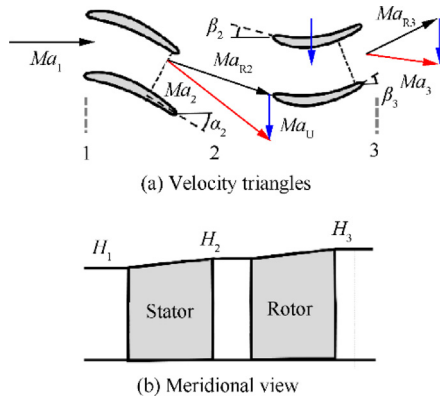
Fig. 14   Turbine stage layout.

4. Stage design and evaluation

4.1. 1D methodology for stage design

In axial supersonic turbines, the downstream conditions are not defined by the outlet static pressure but by the geometry of the passage, inlet conditions, and irreversibility. Let us consider isentropic flows, in a stationary blade row the total temperature at the inlet is identical to the outlet ($T_{0,\text{in}} = T_{0,\text{out}}$), the outlet flow properties can be estimated using Eq. (10):

$$
Ma_{\text{out}} \left(1 + \frac{\gamma - 1}{2} Ma_{\text{out}} \right)^{-0.5\left(\frac{\gamma+1}{\gamma-1}\right)}
$$

$$
= \frac{H_{\text{in}} \cos \alpha_{\text{in}}}{H_{\text{in}} \cos \alpha_{\text{out}}} \cdot \frac{p_{0,\text{in}}}{p_{0,\text{out}}} Ma_{\text{in}} \left(1 + \frac{\gamma - 1}{\gamma} Ma_{\text{in}} \right)^{-0.5\left(\frac{\gamma+1}{\gamma-1}\right)} \quad (10)
$$

In the previous equation, $H_{\text{in}}/H_{\text{out}}$ is the height inlet to outlet ratio. The Kantrowitz self-starting boundary (Eq. (2)) defines the maximum turning, and thus the exit flow angle (α_{out}). Fig. 14(a) sketches the blade-to-blade geometry and defines the angle conventions. Fig. 14(b) displays an axial cut of the turbine passage to illustrate the change of radius along the vane and rotor endwalls. The specific heat ratio and enthalpy were computed at each station along the turbine

utilizing Cantera,[33] chemical kinetics and thermodynamic toolbox, and the $p_{0,\text{in}}/p_{0,\text{out}}$ evaluated with the previously discussed reduced-order loss solver. An iterative procedure was implemented in MATLAB to calculate the outlet Mach number, both in the vane and in the rotor row, using the relative frame of reference. The overall stage work (ΔW_{max}) extraction is evaluated by first computing the conditions isentropically across the stator: $p_{01} = p_{02}$; and then repeating the approach in the rotor the relative rotor inlet total pressure (Plane 2) remains the same at the rotor outlet (Plane 3): $p_{\text{relative},02} = p_{\text{relative},03}$.

4.2. Parametric study on design parameters

Fig. 15(a) maps the specific enthalpy, in the function of the vane outlet flow angle (α_2), the rotor exit flow angle in the relative frame of reference (β_3) for a constant turbine passage height (H). The stator's design space is bounded by the maximum area contraction or outlet stator angle, ensuring a stable supersonic operation. The same is noted for β_3, the ultimate turning in the rotor passage is dictated by the inlet relative rotor angle (β_2) and the inlet velocity in the relative frame of reference (Ma_{R2}) as dictated by the stator design choice. Enlarging α_2 causes more turning, bounding further the maximum inlet Mach number. To respect the Kantrowitz limit, the maximum absolute outlet rotor angle ought to be diminished. Therefore, the maximum power output compromises a balance between α_2 and β_3. With identical inlet velocity, Fig. 15(b) displays the specific enthalpy (Δh) results with a vane channel height increase of 20% from inlet to outlet, $H_2 = 1.2H_1$, and 20% increase along the rotor passage $H_3 = 1.2H_2$. The design space is widened for both vane and the entire turbine stage. The available flow turning on each passage was enhanced with the increase of outlet area. The turning across the vane was increased more than 10°, which in turn also enhanced the rotor range of operation. The increase of 20% in the rotor channel height resulted in nearly doubling the stage specific enthalpy.

Fig. 16(a) depicts the specific power, at three inlet Mach numbers, as a function of the rotational speed (U). Each point along the line is the result of evaluating the optimal

(a) At constant channel height

(b) Increasing channel height by 20% in each row
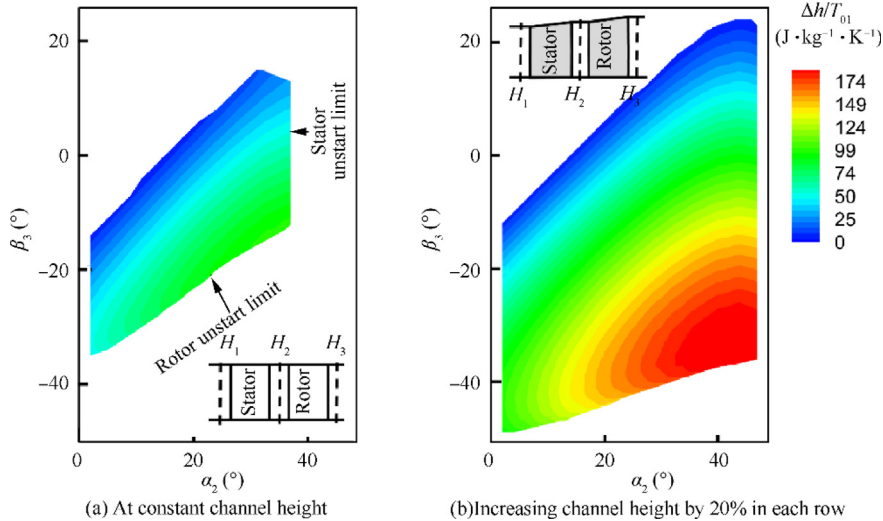
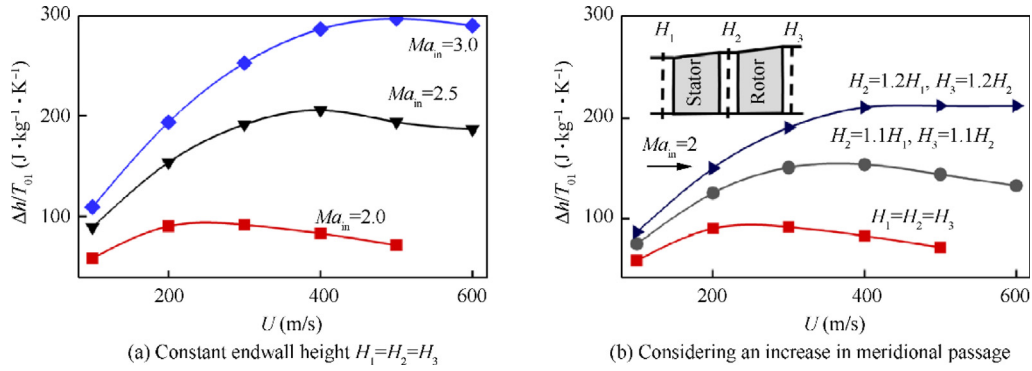**Fig. 15**   Specific enthalpy for different stator outlet angles (α_2) and rotor outlet angle (β_3).

Fig. 16 Specific enthalpy in function of rotational speed (U).

combination of vane outlet (α_2) and rotor outlet flow angle (β_3). We observe a monotonic increase in the specific power with the turbine inlet velocity. Running at Ma_{in} = 2.5 represents an increase of 120% in specific power relative to the baseline Ma_{in} = 2.0 case, due to the higher flow velocities and lower supersonic starting limitations. Based on the Euler equation, the turbine enthalpy is directly propositional to rotational speed. However, a counter effect relates the rotational speed with the amount of possible flow turning across the rotor passage ($\beta_3 - \beta_2$) that ensures a started supersonic flow. For example, when Ma_{in} increased to 2.5 the optimal rotational speed rose by 60%. Thus, there is an ideal revolutions per minute for each operational Mach number. In Fig. 16(b), we compare different growth rates of the turbine passage along the axial direction, 10%, and 20% increase in the height, relative to the constant height. Enlarging the height of the turbine passage along the turbine yields higher specific enthalpy and increases the rotor's optimal rotational speeds. Hence, this analysis/tool provides the necessary correlations to perform a complete engine matching when other turbomachinery components are involved and attached to the same shaft.

The parametric analysis defines the relevant design space conducive to maximum power extraction. Afterward, a complete airfoil optimization can be launched based on direct evaluations of the losses and the isentropic Mach number distribution, using the method of characteristics coupled with an optimization scheme based on genetic algorithms. This meshless design tool was assessed by comparing the results with Reynolds Averaged Navier-Stokes.[20] A reduction in the turbine rotational speed causes positive incidence into the supersonic blading. At the leading-edge, we observe a steeper acceleration along the suction side and a stronger right-running leading-edge shock, which originate a recirculation bubble, abating the turbine performance.[13] Interestingly, the off-design performance of supersonic internal passages is highly dependent on the excitation frequency. At low reduced frequencies, a hysteresis-like behavior is observed between the inlet and the outlet distinct from the steady prediction.[21] At higher reduced frequencies, the inlet flow fluctuations are faster than the traveling time of a characteristic wave between the inlet and outlet planes. Hence, the slowest characteristic waves are overtaken by waves of the opposite family; the amplitudes are significantly damped across the turbine passage.

5. Conclusions

This paper presents both a new approach to optimize axial supersonic turbines suitable for detonation-based engines as well as guidelines for turbine and engine designers. The paper presents first the design space that guarantees the startability of the supersonic passages during the engine starting phase. Secondly, the primary sources of entropy generation were diagnosed. A strategy was explained to evaluate the shock and viscous losses, comprising profile, associated with the boundary layer spread, and mixing loss caused by the shear between the wakes and the core flow. The main cause of irreversibility is the leading-edge bow shock. Shock loss is predominant in high inlet Mach numbers and is responsible for a steep performance decrease with a higher chord to pitch ratio and leading-edge thickness. The results of the reduced-order model were benchmarked against 3D Navier-Stokes simulations at different inlet supersonic velocities and geometrical properties.

Additionally, we used various Navier-Stokes simulations to characterize the downstream flow field and identify the optimal chord to pitch ratio for different operating conditions. The proposed loss models were then combined with an algorithm to determine the vane and rotor outlet flow angles conducive to maximum non-isentropic enthalpy from the single supersonic stage. This approach's low computational demand allowed us to study the impact of different geometrical and operational conditions. We observed that an increase of the meridional passage allows more turning in the stator and rotor. For example, a 20% blade height variation offered a 100% gain in specific power output. Finally, we showed that the optimal peripheral speed increases with the inlet Mach number and the blade height variation. This methodology provides the fundamental steps to guide supersonic turbines' initial design suitable for high-speed inlet conditions. The reduced-order approach is used to estimate the non-isentropic power output from a single stage.

Declaration of Competing Interest

The authors declare that they have no known competing financial interests or personal relationships that could have appeared to influence the work reported in this paper.

Acknowledgments

References

1. Grote M, Williams I, Preston J. Direct carbon dioxide emissions from civil aircraft. *Atmos Environ* 2014;**95**:214–24.
2. Masiol M, Harrison RM. Aircraft engine exhaust emissions and other airport-related contributions to ambient air pollution: A review. *Atmos Environ* 2014;**95**:409–55.
3. Gaspar RMP, Sousa JMM. Impact of alternative fuels on the operational and environmental performance of a small turbofan engine. *Energy Convers Manag* 2016;**130**:81–90.
4. Lee JJ. Can we accelerate the improvement of energy efficiency in aircraft systems? *Energy Convers Manag* 2010;**51**(1):189–96.
5. Ma JZ, Luan MY, Xia ZJ, et al. Recent progress, development trends, and consideration of continuous detonation engines. *AIAA J* 2020;**58**(12):4976–5035.
6. Sousa J, Paniagua G, Collado ME. Thermodynamic analysis of a gas turbine engine with a rotating detonation combustor. *Appl Energy* 2017;**195**:247–56.
7. Heiser WH, Pratt DT. Thermodynamic cycle analysis of pulse detonation engines. *J Propuls Power* 2002;**18**(1):68–76.
8. Alhussan K, Assad M, Penazkov O. Analysis of the actual thermodynamic cycle of the detonation engine. *Appl Therm Eng* 2016;**107**:339–44.
9. Sousa J, Braun J, Paniagua G. Development of a fast evaluation tool for rotating detonation combustors. *Appl Math Model* 2017;**52**:42–52.
10. Mizener AR, Lu FK. Low-order parametric analysis of a rotating detonation engine in rocket mode. *J Propuls Power* 2017;**33**(6):1543–54.
11. Fernelius MH, Gorrell SE. Predicting efficiency of a turbine driven by pulsing flow. New York: ASME; 2017. Report No.: GT2017-63490.
12. Zhou SB, Ma H, Li S, et al. Effects of a turbine guide vane on hydrogen-air rotating detonation wave propagation characteristics. *Int J Hydrog Energy* 2017;**42**(31):20297–305.
13. Paniagua G, Iorio MC, Vinha N, et al. Design and analysis of pioneering high supersonic axial turbines. *Int J Mech Sci* 2014;**89**:65–77.
14. Bedick C, Sisler A, Ferguson DH, et al. Development of a lab-scale experimental testing platform for rotating detonation engine inlets. Reston: AIAA; 2017. Report No.: AIAA-2017-0785.
15. Knowlen C, Wheeler E, Mendez D, et al. Thrusting pressure and supersonic exhaust velocity in a rotating detonation engine. Reston: AIAA; 2018. Report No.: AIAA-2018-0884.
16. Braun J, Saracoglu BH, Paniagua G. Unsteady performance of rotating detonation engines with different exhaust nozzles. *J Propuls Power* 2016;**33**(1):121–30.
17. Schwer D, Kailasanath K. Fluid dynamics of rotating detonation engines with hydrogen and hydrocarbon fuels. *Proc Combust Inst* 2013;**34**(2):1991–8.
18. Liu Z, Braun J, Paniagua G. Thermal power plant upgrade via a rotating detonation combustor and retrofitted turbine with optimized endwalls. *Int J Mech Sci* 2020;**188**:105918.
19. Kantrowitz A, Donaldson CD. Preliminary investigation of supersonic diffusers. Washington, D.C.: NACA; 1945. Report No.: NACA ACR L5D20.
20. Sousa J, Paniagua G. Entropy minimization design approach of supersonic internal passages. *Entropy* 2015;**17**(8):5593–610.
21. Sousa J, Paniagua G, Saavedra J. Aerodynamic response of internal passages to pulsating inlet supersonic conditions. *Comput Fluids* 2017;**149**:31–40.
22. Liu Z, Braun J, Paniagua G. Characterization of a supersonic turbine downstream of a rotating detonation combustor. *J Eng Gas Turbines Power* 2019;**141**(3):031501.
23. Spalart P, Allmaras S. A one-equation turbulence model for aerodynamic flows. Reston: AIAA; 1992. Report No.: AIAA-1992-0439.
24. McBride BJ, Gordon S, Reno MA. Thermodynamic data for fifty reference elements. Washington, D.C.: NASA; 2001. Report No.: NASA/TP-3287.
25. Toro EF, Spruce M, Speares W. Restoration of the contact surface in the HLL-Riemann solver. *Shock Waves* 1994;**4**(1):25–34.
26. Richardson LF. The approximate arithmetical solution by finite differences of physical problems involving differential equations, with an application to the stresses in a masonry dam. *Phil Trans R Soc Lond A* 1911;**210**(459–470):307–57.
27. Celik IB, Ghia U, Roache PJ. Procedure for estimation and reporting of uncertainty due to discretization in CFD applications. *J Fluids Eng* 2008;**130**(7):078001.
28. Moeckel W. Approximate method for predicting form and location of detached shock waves ahead of plane or axially symmetric bodies. Washington, D.C.: NACA; 1949. Report No.: NACA TN D-1921.
29. Stewart WL. Analysis of two-dimensional compressible-flow loss characteristics downstream of turbomachine blade rows in terms of basic boundary-layer characteristics. Washington, D.C.: NACA; 1955. Report No.:NACA-TN-3515.
30. Stratford B, Beavers GS. The calculation of the compressible turbulent boundary layer in an arbitrary pressure gradient: A correlation of certain previous methods. London: Her Majesty's Stationery Office; 1961. Report No.: R. & M. 3207.
31. Senoo S. Development of design method for supersonic turbine aerofoils near the tip of long blades in steam turbines: Part 1—Overall configuration. *Proceedings of ASME turbo expo 2012: Turbine technical conference and exposition*; New York: ASME; 2012. p. 355–65.
32. Dvořák R, Šafařík P, Luxa M, et al. Optimizing the tip section profiles of a steam turbine blading. *Proceedings of ASME 2013 turbine blade tip symposium*; New York: ASME; 2014.
33. Goodwin D, Moffat H, Speth R. Cantera: An object-oriented software toolkit for chemical kinetics, thermodynamics, and transport processes [Internet]. 2018 May 17[cited 2022 Jan 10]. Available from: http://www.cantera.org.
34. Sousa J, Paniagua G, Collado-Morata E. Analysis of the aerodynamic losses in a supersonic turbine. New York: ASME; 2017. Report No.: POWER-ICOPE2017-3624.